

This is the accepted manuscript made available via CHORUS. The article has been published as:

Noise reduction in differential phase extraction of dual atom interferometers using an active servo loop

Sheng-wei Chiow, Jason Williams, and Nan Yu

Phys. Rev. A **93**, 013602 — Published 6 January 2016

DOI: [10.1103/PhysRevA.93.013602](https://doi.org/10.1103/PhysRevA.93.013602)

Noise reduction in differential phase extraction of dual atom interferometers using an active servo loop

Sheng-wei Chiow, Jason Williams, Nan Yu*

Jet Propulsion Laboratory, California Institute of Technology, Pasadena, CA 91109

Differential measurements using simultaneous atom interferometers provide unprecedented precision and stability for explorations on the scientific frontiers. Phase extraction between two atom interferometers, however, imposes additional limitations on the overall instrument performance due to nonlinear multi-parameter fit and associated reduced data rate and sensitivity. We propose an active differential phase extraction method, which is self-calibratable and yields the theoretical performance of differential measurement for uncorrelated errors, and demonstrate the scheme on a transportable gravity gradiometer. The gravity gradient sensitivity of the instrument is improved by a factor of 3 with the implementation of the technique, which is in consistent with independently measured detection noise. We also demonstrate the accuracy and applicability of the scheme to with 33kg test masses, and achieve $1E$ uncertainty after 4000s.

PACS numbers: 37.25.+k, 03.75.Dg, 07.87.+v, 91.10.Pp

Multiple light-pulse atom interferometers coupled with common Bragg or Raman interferometer pulses, so-called simultaneous atom interferometers (AI), have been developed worldwide to exploit the accuracy and sensitivity of atom interferometers, examples include measurements of gravity gradients [1–4], rotation rates [5], the Gravitational constant G [6, 7], the photon recoil frequency to measure \hbar/m [8, 9], gravitational waves [10–14], tests of Einstein’s equivalence principle [15–21], etc. Thanks to the commonality between simultaneous AIs, these instruments theoretically have greatly suppressed sensitivity to common mode noises such as laser phase noise and vibrational noise, which is hard to suppress at low frequencies [22–24]. In practice, the actual performance of these instruments, in addition to the intrinsic noise of each AI such as the quantum projection noise (QPN) of the signal atoms (also known as the atom shot noise [25]), depends heavily on the ability of phase extraction between two AIs.

In an AI, each atom traverses two paths in space-time, thanks to light-pulse matterwave beam splitters that split, reflect, and recombine wave function between two states. The phase difference between two paths is represented by the probability of finding the atom in one state (ground) or the other (excited) after the AI sequence. In general, the outputs of two simultaneous AIs can be expressed in the form:

$$\begin{aligned} s_1 &= a_1 + b_1 \sin(\phi_c + \phi_d) + s_{1,\text{QPN}} \\ s_2 &= a_2 + b_2 \sin(\phi_c) + s_{2,\text{QPN}}, \end{aligned} \quad (1)$$

where s_i is the normalized excitation fraction (NEF) of the readout, a_i, b_i the respective fringe offset and amplitude, ϕ_c the common phase, $s_{i,\text{QPN}}$ the quantum projection noise [7], and ϕ_d the differential phase. ϕ_c represents interferometer sensitivities to, e.g., magnetic fields, grav-

ity, rotation, vibration, and laser phases that are common to both, and ϕ_d represents signals that are not common, arising from gradients, systematics, and perturbations local to one AI. Dual AIs are typically designed to be as similar as possible, including the use of simultaneous operation, common interrogation laser pulse, common retroreflection mirror, common laser wavelength, etc, while maintaining the sensitivity of ϕ_d to the quantity of interest such as gravity gradient and the photon recoil frequency. It is thus a general scenario that at high sensitivity in a noisy environment ϕ_c varies randomly from shot to shot by at least few radians and ϕ_d remains relatively stationary. Efforts have been made to precisely and accurately recover ϕ_d from two random but correlated data sets $\{s_1, s_2\}$ [26–28]. For instance, ellipse-specific fitting utilizes trigonometric identities to eliminate ϕ_c in Eq. (1), resulting in an ellipse equation with its eccentricity determined by ϕ_d [26]. Bayesian analysis estimates the probability of obtaining each data pair (s_1, s_2) as a function of ϕ_d , considering all possible ϕ_c and noise models [27]. Ellipse fitting yields results with excessive noise to the instrument noise, ϕ_d dependent systematic and noise sensitivity, and demanding sufficient data to function properly (e.g., 100 points per ellipse [7]), while Bayesian analysis requires appropriate noise model and could be computation intensive. Adapting mechanical accelerometers for ϕ_c estimation for interferometer fringe locking or for sinusoidal fringe fitting is also performed [4, 28–31].

Here we propose and demonstrate a generally applicable active differential phase extraction method to achieve an overall instrument performance at the level of the quadrature sum of noise from individually interrogated AIs. In this method, a differential phase shift between two AIs is introduced and actively servoed to minimize the phase difference of the AIs. We show that this method is immune from offset and amplitude noise and drifts, thus delivering a sensitivity limited only by the noise of individual AI itself. The immunity comes from the identity of noise distribution under dithering of the

* nan.yu@jpl.nasa.gov

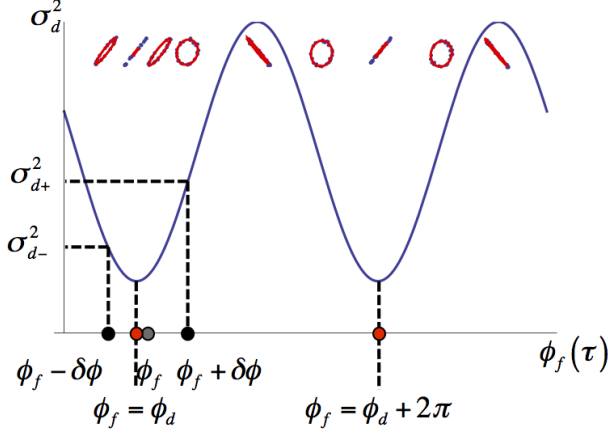


FIG. 1. (Color online) Depiction of the locking scheme. The sinusoidal curve is the variance σ_d^2 (in arbitrary units) as a function of the additional phase ϕ_f (in radian) while ϕ_d is the differential phase to be measured (Eq. (5)). ϕ_f is controlled via a physical parameter τ , which in our demonstration is a pulse duration. At $\phi_f = \phi_d$, σ_d^2 is minimum and $\sigma_{d+}^2 = \sigma_{d-}^2$, thus ϕ_d is measured by ϕ_f when a servo to τ continuously minimizes $|\sigma_{d+}^2 - \sigma_{d-}^2|$. Point $\phi_f(\tau + \tau_{\text{cal}}) = \phi_d + 2\pi$ will be used for self-calibration. Insets on top show parametric plots of experimental data (blue dots) overlaid with the fitted ellipses (red figures) at different ϕ_f . When $\phi_f = \phi_d$, the ellipse is collapsed into a line. The opening of each ellipse is measured by σ_d^2 .

servoed phase on the time scale of dither cycle time, resulting in higher noise rejection bandwidth than conventional methods. The scale factor for the differential phase generation can be self-calibrated to the instrument sensitivity, thus satisfying all operational requirements derived from the instrument sensitivity itself. Moreover, it can be applied to dynamic signal measurements and significantly increase the measurement bandwidth as the method locks two atom interferometers operating near the zero phase crossing points.

The active phase extraction method works as follows. Consider a_i, b_i in Eq. (1) having constant values of \bar{a}_i, \bar{b}_i and fluctuations from measurement (shot) to measurement (shot) a_{iN}, b_{iN} (due to technical noises for example), so that $a_i = \bar{a}_i + a_{iN}$ and $b_i = \bar{b}_i + b_{iN}$. Defining normalized outputs of each shot $X \equiv (s_1 - \bar{a}_1)/\bar{b}_1$ and $Y \equiv (s_2 - \bar{a}_2)/\bar{b}_2$, the variance σ_d^2 of $(X - Y)$ is:

$$\begin{aligned} X - Y = & \left(\frac{a_{1N}}{\bar{b}_1} - \frac{a_{2N}}{\bar{b}_2} \right) + \cos \phi_c \left(1 + \frac{b_{1N}}{\bar{b}_1} \right) \sin \phi_d \\ & + \sin \phi_c \left(\left(1 + \frac{b_{1N}}{\bar{b}_1} \right) \cos \phi_d - \left(1 + \frac{b_{2N}}{\bar{b}_2} \right) \right) \\ & + \frac{s_{1,\text{QPN}}}{\bar{b}_1} - \frac{s_{2,\text{QPN}}}{\bar{b}_2}, \end{aligned} \quad (2)$$

$$\begin{aligned} \sigma_d^2 \equiv & \langle (X - Y)^2 \rangle_{\phi_c} \\ = & \frac{1}{2} \left[\left(1 + \frac{\overline{b_{1N}}}{\bar{b}_1} \right)^2 + \left(1 + \frac{\overline{b_{2N}}}{\bar{b}_2} \right)^2 + \frac{\sigma_{b_1}^2}{\bar{b}_1^2} + \frac{\sigma_{b_2}^2}{\bar{b}_2^2} \right] \\ & + \left(\frac{\overline{a_{1N}}}{\bar{b}_1} - \frac{\overline{a_{2N}}}{\bar{b}_2} \right)^2 + \frac{\sigma_{a_1}^2}{\bar{b}_1^2} + \frac{\sigma_{a_2}^2}{\bar{b}_2^2} \\ & - \left(1 + \frac{\overline{b_{1N}}}{\bar{b}_1} \right) \left(1 + \frac{\overline{b_{2N}}}{\bar{b}_2} \right) \cos \phi_d \\ & + \frac{2\bar{a}'_1(1 - \bar{a}'_1) - \bar{b}_1'^2}{2\bar{b}_1^2 N_{1,\text{atom}}} + \frac{2\bar{a}'_2(1 - \bar{a}'_2) - \bar{b}_2'^2}{2\bar{b}_2^2 N_{2,\text{atom}}}, \end{aligned} \quad (3)$$

where $\langle \cdot \rangle_{\phi_c}$ is the ensemble average over ϕ_c , the noise terms a_{iN}, b_{iN} are uncorrelated with respective variance $\sigma_{\{a_i, b_i\}}^2$, $\bar{a}'_i = \bar{a}_i + \overline{a_{iN}}$, $\bar{b}'_i = \bar{b}_i + \overline{b_{iN}}$, and $N_{i,\text{atom}}$ the mean atom number in each AI. The means $\overline{a_{iN}}, \overline{b_{iN}}$ account for deviations of \bar{a}_i, \bar{b}_i from the true average values. Note that if \bar{a}_i, \bar{b}_i are the means of a_i, b_i , then $\overline{a_{iN}} = \overline{b_{iN}} = 0$, $\bar{a}'_i = \bar{a}_i$, $\bar{b}'_i = \bar{b}_i$. When $\phi_d, \overline{a_{iN}}, \overline{b_{iN}}$ are small, Eq. (3) can be approximated as

$$\begin{aligned} \sigma_d^2 \approx & \frac{2\sigma_{a_1}^2 + \sigma_{b_1}^2}{2\bar{b}_1^2} + \frac{2\sigma_{a_2}^2 + \sigma_{b_2}^2}{2\bar{b}_2^2} + \frac{\phi_d^2}{2} \\ & + \frac{\sigma_{1,\text{QPN}}^2}{\bar{b}_1^2} + \frac{\sigma_{2,\text{QPN}}^2}{\bar{b}_2^2} + \mathcal{O}(\overline{a_{iN}}, \overline{b_{iN}}, \dots), \end{aligned} \quad (4)$$

where $\mathcal{O}(\dots)$ includes terms dependent on $\overline{a_{iN}}, \overline{b_{iN}}$, and $\sigma_{i,\text{QPN}}^2/\bar{b}_i^2 = (2\bar{a}'_i(1 - \bar{a}'_i) - \bar{b}_i'^2)/2\bar{b}_i^2 N_{i,\text{atom}}$ are the corresponding QPN terms [7]. In our active phase extraction method, an additional phase shift ϕ_f is introduced in only one of the interferometers, so that Eqs. (1) and (4) are modified $\phi_d \rightarrow \phi_d - \phi_f$:

$$\begin{aligned} \sigma_d^2 \approx & \frac{2\sigma_{a_1}^2 + \sigma_{b_1}^2}{2\bar{b}_1^2} + \frac{2\sigma_{a_2}^2 + \sigma_{b_2}^2}{2\bar{b}_2^2} + \frac{(\phi_d - \phi_f)^2}{2} \\ & + \frac{\sigma_{1,\text{QPN}}^2}{\bar{b}_1^2} + \frac{\sigma_{2,\text{QPN}}^2}{\bar{b}_2^2} + \mathcal{O}(\overline{a_{iN}}, \overline{b_{iN}}, \dots). \end{aligned} \quad (5)$$

The phase extraction of dual AI is thus converted from a data analysis problem to a task of active minimization of σ_d^2 by varying ϕ_f .

Locking to the minimum of σ_d^2 is achieved by dithering ϕ_f , as illustrated in Fig. 1, where σ_d^2 is measured at two values of $\phi_f \pm \delta\phi$. The difference $(\phi_d - \phi_f)$ is proportional to $(\sigma_{d+}^2 - \sigma_{d-}^2)$:

$$\begin{aligned} \sigma_{d\pm}^2 \approx & \frac{2\sigma_{a_1}^2 + \sigma_{b_1}^2}{2\bar{b}_1^2} + \frac{2\sigma_{a_2}^2 + \sigma_{b_2}^2}{2\bar{b}_2^2} + \frac{(\phi_d - (\phi_f \pm \delta\phi))^2}{2} \\ & + \frac{\sigma_{1,\text{QPN}}^2}{\bar{b}_1^2} + \frac{\sigma_{2,\text{QPN}}^2}{\bar{b}_2^2} + \mathcal{O}(\dots) \\ \Delta\sigma_d^2 \equiv & \sigma_{d+}^2 - \sigma_{d-}^2 \approx -2(\phi_d - \phi_f)\delta\phi, \end{aligned} \quad (6)$$

assuming both $(\phi_d - \phi_f)$ and $\delta\phi$ are small. $\Delta\sigma_d^2$ serves as the error signal for the active locking loop. When $(\phi_d - \phi_f)$ is large, the approximate expression Eq. (6) does not hold, however, the algorithm still works as $(\phi_d - \phi_f)$ is

Simulation Run	A	B	C	D	E	F	G	H	I	J
Fringe amplitude \bar{b}	0.5	0.25	0.5	0.25	0.25	0.25	0.5	0.25	0.25	0.25
Detection noise σ_a (10^{-3})	0	0	3	1	3	10	0	0	0	0
Contrast noise σ_b (10^{-3})	0	0	0	0	0	0	3	1	3	10
Fundamental noise at 1s (mrad) (active phase extraction noise)	1.4	3.7	12	8	24	80	8.5	5.7	17	57
Fit noise at 1s (mrad)	1.8	4.4	16.5	12.0	43.8	122	12.4	11.3	33	121
Ellipse fitting degradation	1.3	1.2	1.4	1.5	1.8	1.5	1.5	2.0	1.9	2.1

TABLE I. Ellipse fitting simulation results. $\phi_d = 1.32$ rad, 20 points per ellipse. All simulation runs include QPN of 10^6 atoms in each AI and 10000 pairs of data. Fringe offset is $\bar{a} = 0.5$. Fundamental noise is the theoretical phase resolution limited only by the sensitivity to the noise sources. Note that the active phase extraction method reaches this fundamental noise, as shown in Eq. (8). The ellipse fitting degradation is defined as the ratio of the fit noise to the fundamental noise.

slowly pulled-in towards the lock point. Note that the error signal in Eq. (6) does not contain the amplitude and offset deviations (\bar{a}_{iN} and \bar{b}_{iN}) and noises ($\sigma_{a_i}^2, \sigma_{b_i}^2$ and $\sigma_{i,\text{QPN}}^2$). The immunity comes from the identity of noise distribution under dithering of ϕ_f , which is valid so long as the noise characteristics are consistent between $\phi_f \pm \delta\phi$. Similar conclusion can be derived for other noise sources not captured in Eq. (5).

This noise immunity, however, does not suggest performance beyond QPN or any noise source discussed above. It is understood that sufficient data are required to obtain accurate measurements of $\sigma_{d\pm}$, \bar{a}_i , and \bar{b}_i . The accuracy is expected to improve as $1/\sqrt{N_E}$ where N_E is the size of the ensemble, which in practice is minimized to increase the update rate of ϕ_f in order to achieve fast settling and to be on a timescale that is fast with respect to drifts in \bar{a}_i, \bar{b}_i , even the variation of ϕ_d itself. Thus, $\Delta\sigma_d^2$ obtained in a limited time has $1/N_E$ suppressed sensitivity to $\bar{a}_i, \bar{b}_i, \sigma_{a_i}^2, \sigma_{b_i}^2$, and other noises. Additionally, $\Delta\sigma_d^2$ carries residuals of cross terms of $\sin\phi_c, \cos\phi_c, \sin\phi_c \cos\phi_c$ in evaluating Eq. (6) from Eq. (2) due to averaging over finite ensemble, which are proportional to $\delta\phi$ to the leading order when $\phi_f \approx \phi_d$:

$$\begin{aligned}
\Delta\sigma_d^2 \approx & -2(\phi_d - \phi_f)\delta\phi \\
& + \frac{1}{N_E} \left(\frac{2\sigma_{a_1}^2 + \sigma_{b_1}^2}{2\bar{b}_1^2} + \frac{2\sigma_{a_2}^2 + \sigma_{b_2}^2}{2\bar{b}_2^2} \right) \\
& + \frac{1}{N_E} \left(\frac{\sigma_{1,\text{QPN}}^2}{\bar{b}_1^2} + \frac{\sigma_{2,\text{QPN}}^2}{\bar{b}_2^2} \right) \\
& + \frac{\delta\phi}{N_E} (\dots) + \frac{1}{N_E} \mathcal{O}(\dots). \tag{7}
\end{aligned}$$

Note that the sensitivity to amplitude and offset drifts, captured in \bar{a}_{iN} and \bar{b}_{iN} , is also suppressed as $1/N_E$. The expression of finite ensemble variance in Eq. (7) leads to a noise figure consistent with the anticipated instrument performance for independent errors.

To have estimate at times much shorter than the servo attack time, we define $\Delta\phi \equiv \sqrt{2}(X - Y)$ (X, Y as in Eq. (2)) as the instantaneous estimate of $(\phi_d - (\phi_f \pm \delta\phi))$ for statistics purposes. The variance of $\Delta\phi$ (following

Eq. (6)) is

$$\begin{aligned}
\langle \Delta\phi^2 \rangle &= \frac{1}{N_E} \sum \Delta\phi^2 \xrightarrow{N_E \rightarrow \infty} 2\sigma_{d\pm}^2 \\
&\approx \frac{2\sigma_{a_1}^2 + \sigma_{b_1}^2}{\bar{b}_1^2} + \frac{2\sigma_{a_2}^2 + \sigma_{b_2}^2}{\bar{b}_2^2} \\
&\quad + \frac{2\sigma_{1,\text{QPN}}^2}{\bar{b}_1^2} + \frac{2\sigma_{2,\text{QPN}}^2}{\bar{b}_2^2} \\
&\quad + (\phi_d - (\phi_f \pm \delta\phi))^2. \tag{8}
\end{aligned}$$

In the noise free situation, $\langle \Delta\phi^2 \rangle \rightarrow (\phi_d - (\phi_f \pm \delta\phi))^2$, which justifies the definition of $\Delta\phi$. With the presence of noise, for instance the QPN, $\langle \Delta\phi^2 \rangle$ reaches the sensitivity limited by the standard QPN: On the one hand, the QPN limits the sensitivity of differential AIs at $\sqrt{2} \times \sqrt{2}(\sigma_{\text{QPN}}/\bar{b})$, where one $\sqrt{2}$ accounts for reduced sensitivity from random phase ϕ_c , the other $\sqrt{2}$ for taking difference between two AIs, and $\sigma_{\text{QPN}}/\bar{b}$ represents the QPN-limited phase resolution of each AI on fringes of amplitude \bar{b} . On the other hand, Eq. (8) yields $\langle \Delta\phi^2 \rangle \rightarrow 4\sigma_{\text{QPN}}^2/\bar{b}^2 + \delta\phi^2$, with $\sigma_{a_1} = \sigma_{a_2} = \sigma_a, \sigma_{b_1} = \sigma_{b_2} = 0, \bar{b}_1 = \bar{b}_2 = \bar{b}, \sigma_{1,\text{QPN}} = \sigma_{2,\text{QPN}} = \sigma_{\text{QPN}}, \phi_d = \phi_f$.

To compare with the widely used ellipse-specific fitting method, a numerical simulation using ellipse fitting for phase extraction was performed based on typical experimental conditions. A set of $\{s_1, s_2\}$ is generated according to Eq. (1), with $\phi_d = 1.32$ rad and uniformly distributed ϕ_c . ϕ_d is calculated for every 10 or 20 data pairs using the ellipse-specific fitting algorithm [26], and the phase uncertainty of this data set is determined by extrapolating the Allan deviation of the ϕ_d series to 1s (assuming a 1Hz data rate). Table I shows the results of simulation, where technical noise σ_a (referred to as detection noise hereafter) other than a QPN corresponding to 10^6 atoms is added under various fringe amplitude \bar{b} and a fixed mean offset $\bar{a}_i = 0.5$. The fundamental noise is the quadrature sum of the detection noise and the QPN $2\sqrt{\sigma_a^2 + \sigma_b^2/2 + \sigma_{\text{QPN}}^2}/\bar{b}$. Fit results of Runs C-F, where detection noise is introduced, are roughly factor of 1.5 noisier than the fundamental noise. Simulation results of decreased sensitivity with the ellipse fitting technique

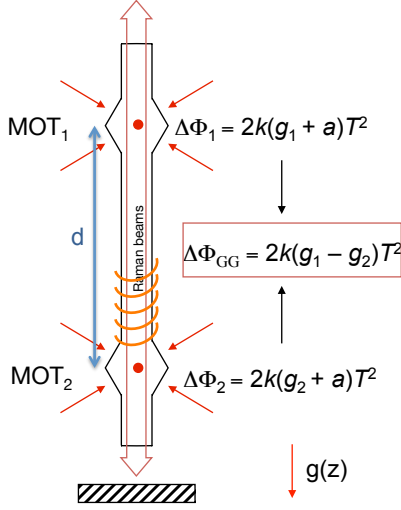


FIG. 2. (Color online) Schematic of the apparatus. $d \approx 1\text{m}$. The retroreflection mirror at the bottom is common to both AIs. k : the Raman laser wavenumber, a : the acceleration of the retroreflection mirror, g_i : the gravitational acceleration at each location. T : the pulse separation time of the AIs. The solenoid in the lower fountain region provides differential phase ϕ_f between AIs to match and thus measure gravity gradient induced phase $\phi_d = 2k(g_1 - g_2)T^2$.

are also reported in Ref. [7]. In the presence of contrast noise instead of detection noise, Runs G-H, more excessive noise of ellipse fitting further limits the performance of such an instrument. In contrasting to the performance of active phase extraction method, which is limited by individual AI noise as shown in Eq. (8) (also listed as the fundamental noise in Table I), clearly the active method is advantageous over the ellipse fitting method, especially when technical noises dominate the noise budget.

Regarding the size of modulation $\delta\phi$, Equation (7) shows that larger modulation amplitude of $\delta\phi$ produces larger error signal (the first term), but also comes with larger residual noise (the third term). It is optimal to choose $\delta\phi$ on the same order as the combined noise. Moreover, small $\delta\phi$ allows measurements in more dynamic environments, such as gravity mapping in space where every measurement is precious and real-time read-out is crucial. From Eq. (2) with ϕ_d replaced by $\phi_d - (\phi_f \pm \delta\phi)$, for $|\delta\phi| \ll |\phi_d - \phi_f| \ll 1$, $(X - Y) \approx (\phi_d - \phi_f) \cos \phi_c$ and $(X + Y)/2 \approx \sin \phi_c$. With additional partial information of ϕ_c from, e.g., a mechanical accelerometer, or vibrational noise compensation by interrogation laser phase manipulation [4, 28–31], $\cos \phi_c$ can be estimated from $(X + Y)/2$ and thus obtaining $\phi_d - \phi_f$ every single shot.

We demonstrate the active phase extraction scheme on a dual cesium fountain apparatus, which is briefly described as follows (Fig. 2). The apparatus was designed as a transportable quantum gravity gradiometer for a technology development and demonstration for

Earth gravity mapping in space. Two simultaneous Cs fountains are vertically separated by 1m and are hosted in a single ultra-high vacuum chamber. Cs atoms are collected in 3D magneto-optical traps (MOT) fed by 2D MOTs for about 350ms, and then the clouds are launched vertically using moving optical molasses. Each AI region is magnetically shielded and has two layers independent solenoids wound between the shielding and the chamber for magnetic bias field control. After the clouds enter the shielded regions, three two-photon Raman pulses are applied to form simultaneous Mach-Zehnder AIs with the pulse separation time $T \leq 165\text{ms}$. When the clouds fall back to the respective trapping regions, AI outputs are read out using fluorescence detection. Two detection pulses are applied to detect atoms in the $F = 4$ state (N_4) and atoms in both the $F = 3$ and $F = 4$ states (N_{3+4}) using a repumping pulse between the detection pulses. NEF of the upper AI output is $s_1 = N_4/N_{3+4}$, while the NEF of the lower AI output is s_2 .

The additional phase shift ϕ_f is introduced and controlled by a pulse of electric current to the second solenoid in the lower AI region, while the first solenoids of both regions are connected in series and fed with a constant current to supply a common bias magnetic field throughout the active regions of the atomic fountains [24, 26]. The current pulse is applied 10ms after the first AI pulse, and is driven by a bipolar operational power supply in externally controlled constant current mode. The external control voltage is provided by a computer controlled pulse generator with the output set to 2V when activated. The pulse duration τ , as required in the active method, is modulated every shot, $\tau_{\pm} = \tau_c \pm \delta\tau$, which is dictated by a LabVIEW servo routine.

The servo for active phase extraction is implemented as follows. At the beginning of a run, τ_c is set at few ms, either using best known value or an arbitrary number, and $\delta\tau = 100\mu\text{s}$. $\tau = \tau_{\pm}$ is updated every shot, and $s_{1,2}$ are measured. After 5 shots on each setting of τ_{\pm} , $\sigma_{d\pm}^2$ is calculated for respective data set using default values $\bar{a}_i = 0.5, \bar{b}_i = 0.2$. A correction proportional to $\sigma_{d+}^2 - \sigma_{d-}^2$ is added to τ_c as the new τ_c for the next 10 shots. The process then repeats with the updated τ_c . After the first 100 shots, offsets and amplitudes start to be estimated from the data themselves: Before τ_c is to be updated, previous 100 data pairs of (s_1, s_2) is taken for estimating \bar{a}_i, \bar{b}_i . For \bar{b}_i , we take the mean of top 5% of s_i as the fringe maximum, the mean of bottom 5% of s_i as the fringe minimum, and $2\bar{b}_i = (\max_i - \min_i)/(\max_i + \min_i)$. This approach is adapted to mitigate nonuniform distribution of ϕ_c (thus s_i) due to the low vibration environment, which renders it ineffective to estimate amplitude from the root-mean-square of a smeared-out fringe. The \bar{a}_i is similarly estimated as $\bar{a}_i = (\max_i + \min_i)/2$. Note that the upper and lower AIs can have different offsets and amplitudes, while τ_{\pm} share the same \bar{a}_i, \bar{b}_i .

As the process progresses, σ_d^2 becomes small due to the locking of the AIs. We program the LabVIEW routine to reduce $\delta\tau$ from $100\mu\text{s}$ to $10\mu\text{s}$ when $\sigma_d \leq 0.03$ to

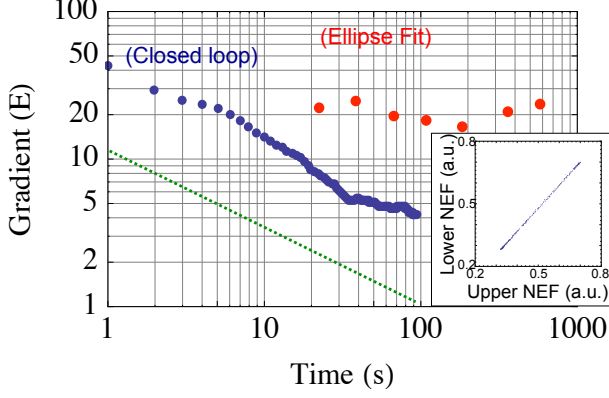


FIG. 3. (Color online) Allan deviation plot of in-loop error signal $\Delta\phi$ when lock is acquired. Inset: Parametric plot of upper and lower NEFs of the same data set. Ellipse fitting data are a typical data set without active feedback. Note that the ellipse fitting data start at 20s, corresponding to the time required to acquire 20 data points for each ellipse. The long term instability of ellipse fit is due to amplitude and offset drifts of AI fringes.

facilitate the small modulation scheme discussed earlier. $\delta\tau = 10\mu\text{s}$ corresponds to $\delta\phi \sim 10\text{mrad}$, which is comparable to our detection noise and \bar{b}_i . When $\sigma_d > 0.1$, on the other hand, it is switched back to large $\delta\tau$ mode, to accommodate sudden changes of ϕ_d or other disruptions.

The conversion coefficient of τ to ϕ_d is critical for the performance of this scheme. In fact, both the common static bias field and the pulsed field affect the scale factor in our approach. We implement a self-calibration method with sensitivity and accuracy limited by the instrument itself. The AI phase due to the quadratic Zeeman shift of magnetic field B is

$$\Phi_B = \alpha B^2 t,$$

where $\alpha = 2\pi \times 427.45\text{Hz/G}^2$ for cesium and t is the duration of interaction. In our scheme, the differential phase between two AIs is

$$\begin{aligned} \phi_f \equiv \Delta\Phi_B &= \alpha [(B_0 + \delta B)^2 - B_0^2] \tau \\ &\approx 2\alpha B_0 \delta B \tau \\ &\equiv C \tau, \end{aligned} \quad (9)$$

where B_0 is the common bias field and δB is the additional field produced by the second solenoid in the lower chamber. Instead of directly evaluating the scale factor C with magnetic field calibrations and precision measurement of α , we experimentally measure it by extending τ_c to $\tau_c + \tau_{\text{cal}}$ so that the two AIs are in phase again (Fig. 1):

$$\phi_f + 2\pi = C(\tau_c + \tau_{\text{cal}}). \quad (10)$$

We then have $C = 2\pi/\tau_{\text{cal}}$. Using larger multiple of 2π for calibration can further increase the sensitivity in determining C , which eventually will be limited by the linearity of Eq. (9) for long τ . The self-calibration is

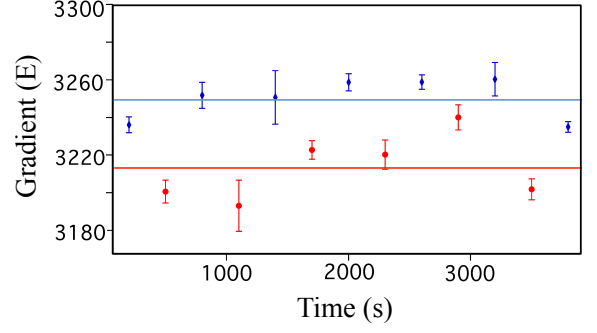


FIG. 4. (Color online) Gravity gradient under mass modulation. Blue diamonds indicate data without extra mass, while red circles for data with lead mass. Each point is an average of ~ 300 data points after the system settles to the new test mass position. Horizontal lines show the weighted average of all measurements at same position.

easily done with our software implementation: After the lock is acquired, an impulse of $\sim 6\text{ms}$ is added to τ_c manually and the system acquires lock again after few updates of τ_c . τ_{cal} is then the difference of the two locked τ_c , which would have comparable resolution and accuracy as the instrument itself. In our apparatus, $C \approx 1\text{rad/ms}$ at a specific B_0 setting. Furthermore, the stability of the electric currents for generating B_0 and δB is also measured and found better than one part per thousand over 24 hours under typical operating conditions, which can be further improved with dedicated electronics when needed.

With the active phase extraction method, we achieve a sensitivity of gravity gradient of $40E/\sqrt{\text{Hz}}$ ($1E = 10^{-9}/\text{s}^2$), with $T = 165\text{ms}$ and cycle time $\sim 1\text{s}$. Typical Allan deviation of $\Delta\phi$ goes down as $1/\sqrt{\tau}$ (Fig. 3), and the value at 1s is taken for the noise spectral density. The in-loop error signal is representative of short-term stability due to limited servo bandwidth. This sensitivity is consistent with our detection noise limited performance of $2\sigma_N/\bar{b} \times 2500E/\text{rad}$, where $\sigma_N \approx 1.6 \times 10^{-3}$ [32], $\bar{b} \approx 0.2$ (equivalent to a fringe contrast of 40%), and $2500E/\text{rad}$ the sensitivity of the 1m baseline gradiometer using 852nm interrogating laser with $T = 165\text{ms}$ in our system. As a comparison, we could at best achieve $120E/\sqrt{\text{Hz}}$ with the traditional ellipse-fitting method. The improvement in instrument sensitivity supports the claimed immunity of the active phase extraction method on the fluctuation and slow variation offset and amplitude, which are major limiting factors of differential AIs using ellipse fitting.

To validate further the calibration and true instrument sensitivity, we perform proximity modulation of $\approx 33\text{kg}$ of test mass while the active locking is engaged, which also demonstrates the applicability of this method to dynamic signals. The test mass is constituted of two lead bricks on top of three lead bricks with minimum gap between them. After the instrument acquired lock, the test mass is manually brought to ≈ 0.5 inches away from the side

of the 2.5-inch diameter vacuum chamber, at the height halfway between the two MOT regions. The instrument starts to respond to the change and settles to a new τ_c in ~ 100 s. After sufficient data are taken (~ 300 s) at this position, the test mass is manually moved away at least 5m from the vacuum chamber. Another settling and data taking phases take place afterwards. The relocation of test mass is typically under 60s. Data shown in Fig. 4 are 7 cycles of mass modulation, where data during relocation and settling are removed. We observe clear modulation of $36.4(1.0)E$ in 4000s. We model the mass distribution and estimate a signal of $34.4(4.0)E$ from the test mass modulation, uncertainty dominated by ~ 1 cm positioning precision. The measured mean and uncertainty are both in agreement with the $40E/\sqrt{\tau}$ in-loop sensitivity.

In summary, we propose and demonstrate an active differential phase extraction method for dual atom interferometers. The method mitigates the degradation of precision and accuracy associated with conventional ellipse fitting methods from otherwise detection noise limited performance. It can be implemented by, e.g., dif-

ferential bias magnetic field as we demonstrated, interrogation laser phases for dissimilar AIs such as conjugate AIs for \hbar/m measurements, light shifts, DC Stark shifts, etc. In addition, the scale factor of this method can be self-calibrated in-operation with uncertainty down to the instrument sensitivity, which guarantees the overall performance of the instrument. The active differential phase extraction method is also relatively immune to instrument performance variations, e.g., offset and contrast change, due to environmental causes, and is capable of capturing dynamic differential signals. This feature greatly enhances the bandwidth and thus the applicability for field applications using differential atom interferometers.

The authors would like to acknowledge Thierry Botter, James Kellogg, James Kohel, David Aveline, and Robert Thompson for their contributions to the development of the transportable quantum gravity gradiometer. This work was carried out at the Jet Propulsion Laboratory, California Institute of Technology, under a contract with the National Aeronautics and Space Administration. © 2015 California Institute of Technology. Government sponsorship acknowledged.

-
- [1] N. Yu, J. M. Kohel, J. R. Kellogg, and L. Maleki. Development of an atom-interferometer gravity gradiometer for gravity measurement from space. *Applied Physics B*, 84(4):647–652, 2006.
 - [2] Nan Yu, James Kohel, Larry Romans, and Lute Maleki. Quantum gravity gradiometer sensor for earth science applications. *NASA Earth Science and Technology Conference 2002. Paper B3P5. Pasadena, California.*, 2002.
 - [3] G. Rosi, L. Cacciapuoti, F. Sorrentino, M. Menchetti, M. Prevedelli, and G. M. Tino. Measurement of the gravity-field curvature by atom interferometry. *Phys. Rev. Lett.*, 114:013001, Jan 2015.
 - [4] Xiao-Chun Duan, Min-Kang Zhou, De-Kai Mao, Hui-Bing Yao, Xiao-Bing Deng, Jun Luo, and Zhong-Kun Hu. Operating an atom-interferometry-based gravity gradiometer by the dual-fringe-locking method. *Phys. Rev. A*, 90:023617, Aug 2014.
 - [5] J K Stockton, K Takase, and M A Kasevich. Absolute geodetic rotation measurement using atom interferometry. *Phys Rev Lett*, 107(13):133001, Sep 2011.
 - [6] J B Fixler, G T Foster, J M McGuirk, and M A Kasevich. Atom interferometer measurement of the Newtonian constant of gravity. *Science*, 315(5808):74–7, Jan 2007.
 - [7] F Sorrentino, Q Bodart, L Cacciapuoti, Y-H Lien, M Prevedelli, G Rosi, L Salvi, and GM Tino. Sensitivity limits of a raman atom interferometer as a gravity gradiometer. *Physical Review A*, 89(2):023607, 2014.
 - [8] Shau-Yu Lan, Pei-Chen Kuan, Brian Estey, Damon English, Justin M. Brown, Michael A. Hohensee, and Holger Müller. A clock directly linking time to a particle’s mass. *Science*, 339(6119):554–557, 2013.
 - [9] Sheng-wei Chiow, Sven Herrmann, Steven Chu, and Holger Müller. Noise-immune conjugate large-area atom interferometers. *Phys Rev Lett*, 103(5):050402, Jul 2009.
 - [10] Savas Dimopoulos, Peter W Graham, Jason M Hogan, Mark A Kasevich, and Surjeet Rajendran. Atomic gravitational wave interferometric sensor. *Physical Review D*, 78(12):122002, 2008.
 - [11] Jason M. Hogan and Mark A. Kasevich. Atom interferometric gravitational wave detection using heterodyne laser links. *arXiv:1501.06797*, Jan 2015.
 - [12] Peter W Graham, Jason M Hogan, Mark A Kasevich, and Surjeet Rajendran. New method for gravitational wave detection with atomic sensors. *Phys Rev Lett*, 110(17):171102, Apr 2013.
 - [13] Nan Yu and Massimo Tinto. Gravitational wave detection with single-laser atom interferometers. *General Relativity and Gravitation*, 43:1943–1952, 2011.
 - [14] Jason M. Hogan, David M. S. Johnson, Susannah Dickerson, Tim Kovachy, Alex Sugarbaker, Sheng-wei Chiow, Peter W. Graham, Mark A. Kasevich, Babak Saif, Surjeet Rajendran, Philippe Bouyer, Bernard D. Seery, Lee Feinberg, and Ritva Keski-Kuha. An atomic gravitational wave interferometric sensor in low earth orbit (AGIS-LEO). *General Relativity and Gravitation*, 43(7):1953–2009, 2011.
 - [15] Brett Altschul, Quentin G Bailey, Luc Blanchet, Kai Bongs, Philippe Bouyer, Luigi Cacciapuoti, Salvatore Capozziello, Naceur Gaaloul, Domenico Giulini, Jonas Hartwig, et al. Quantum tests of the einstein equivalence principle with the ste-qwest space mission. *Advances in Space Research*, 55(1):501–524, 2015.
 - [16] Jason M. Hogan, David M. S. Johnson, and Mark A. Kasevich. Light-pulse atom interferometry. *arXiv:0806.3261*, Jun 2008.
 - [17] A Bonnin, N Zahzam, Y Bidel, and A Bresson. Simultaneous dual-species matter-wave accelerometer. *Physical Review A*, 88(4):043615, 2013.

- [18] Sebastian Fray and Martin Weitz. Atom-based test of the equivalence principle. *Space science reviews*, 148(1-4):225–232, 2009.
- [19] Lin Zhou, Shitong Long, Biao Tang, Xi Chen, Fen Gao, Wencui Peng, Weitao Duan, Jiaqi Zhong, Zongyuan Xiong, Jin Wang, Yuanzhong Zhang, and Mingsheng Zhan. Test of equivalence principle at 10^{-8} level by a dual-species double-diffraction raman atom interferometer. *Phys. Rev. Lett.*, 115:013004, Jul 2015.
- [20] Dennis Schlippert, Jonas Hartwig, Henning Albers, Logan L Richardson, Christian Schubert, Albert Roura, Wolfgang P Schleich, Wolfgang Ertmer, and Ernst M Rasel. Quantum test of the universality of free fall. *Physical Review Letters*, 112(20):203002, 2014.
- [21] MG Tarallo, T Mazzoni, N Poli, DV Sutyryn, X Zhang, and GM Tino. Test of einstein equivalence principle for 0-spin and half-integer-spin atoms: Search for spin-gravity coupling effects. *Physical review letters*, 113(2):023005, 2014.
- [22] J Le Gouët, P Cheinet, J Kim, D Holleville, A Clairon, A Landragin, and F Pereira Dos Santos. Influence of lasers propagation delay on the sensitivity of atom interferometers. *The European Physical Journal D-Atomic, Molecular, Optical and Plasma Physics*, 44(3):419–425, 2007.
- [23] Joel M Hensley, Achim Peters, and Steven Chu. Active low frequency vertical vibration isolation. *Review of scientific instruments*, 70(6):2735–2741, 1999.
- [24] J. M. McGuirk, G. T. Foster, J. B. Fixler, M. J. Snadden, and M. A. Kasevich. Sensitive absolute-gravity gradiometry using atom interferometry. *Physical Review A*, 65(3), 2002.
- [25] WM Itano, JC Bergquist, JJ Bollinger, JM Gilligan, DJ Heinzen, FL Moore, MG Raizen, and DJ Wineland. Quantum projection noise: Population fluctuations in two-level systems. *Physical Review A*, 47(5):3554, 1993.
- [26] G T Foster, J B Fixler, J M McGuirk, and M A Kasevich. Method of phase extraction between coupled atom interferometers using ellipse-specific fitting. *Opt Lett*, 27(11):951–3, Jun 2002.
- [27] John K. Stockton, Xinan Wu, and Mark A. Kasevich. Bayesian estimation of differential interferometer phase. *Physical Review A*, 76(3), 2007.
- [28] B Barrett, L Antoni-Micollier, L Chichet, B Battelier, P-A Gominet, A Bertoldi, P Bouyer, and A Landragin. Correlative methods for dual-species quantum tests of the weak equivalence principle. *arXiv preprint arXiv:1503.08423*, 2015.
- [29] Nan Yu and Lute Maleki. Atomic references for measuring small accelerations. *NASA Tech Briefs*, February 27 2009.
- [30] F. Pereira Dos Santos. Differential phase extraction in an atom gradiometer. *Physical Review A*, 91(6), 2015.
- [31] Jean Lautier, Laurent Volodimer, Thomas Hardin, Sebastien Merlet, Michel Lours, F Pereira Dos Santos, and Arnaud Landragin. Hybridizing matter-wave and classical accelerometers. *Applied Physics Letters*, 105(14):144102, 2014.
- [32] The detection noise is independently measured using open AIs that the third AI pulse is delayed by 1ms. The NEF fluctuation due to AI interference is greatly suppressed by the delay. The measured variation of NEF is then regarded as the intrinsic detection noise of the system.